

## Article

# Metamorphic Evolution of the Archean Supracrustal Rocks from the Qingyuan Area of the Northern Liaoning Terrane, North China Craton: Constrained Using Phase Equilibrium Modeling and Monazite Dating

Ting Liu <sup>1</sup>, Zhuang Li <sup>2,\*</sup> and Chunjing Wei <sup>3</sup><sup>1</sup> College of Earth Sciences, Chengdu University of Technology, Chengdu 610059, China<sup>2</sup> College of Geosciences, China University of Petroleum (Beijing), Beijing 102249, China<sup>3</sup> MOE Key Laboratory of Orogenic Belts and Crustal Evolution, School of Earth and Space Sciences, Peking University, Beijing 100871, China

\* Correspondence: lizhuangcc@pku.edu.cn

**Abstract:** Archean supracrustal rocks from the Qingyuan area of the northern Liaoning terrane, the North China Craton, occur as enclaves or rafts of various scales within tonalite–trondhjemite–granodiorite (TTG) domes. They were normally subjected to metamorphism at amphibolite facies with locally granulite facies. We collected biotite two-feldspar gneiss from the Hongtoushan of the Qingyuan area and conducted petrography, mineral chemistry, phase equilibrium modeling and monazite dating to reveal its metamorphic evolution. The peak condition was constrained to be 750–775 °C at ~7 kbar based on the stability of the inferred peak mineral assemblage and mineral compositions including the pyrite and grossular contents in the garnet core, and  $X_{Mg}$  in biotite. The final condition was constrained to be ~700 °C at ~6 kbar on the solidus based on the presence of muscovite in the final assemblage. The post-peak near-isobaric cooling process was consistent with the core→rim decreasing pyrite content in garnet. Monazite dating yielded a metamorphic age of ~2.50 Ga for the sample, coeval with the final magmatism of TTGs in the terrane. By combining other geological features, we suggest a vertical sagduction process to be responsible for the metamorphic evolution of the Qingyuan area. This process may be correlated with Archean mantle plume.

**Keywords:** archean supracrustal rocks; the Qingyuan area; the north China craton; metamorphic evolution; monazite dating



**Citation:** Liu, T.; Li, Z.; Wei, C. Metamorphic Evolution of the Archean Supracrustal Rocks from the Qingyuan Area of the Northern Liaoning Terrane, North China Craton: Constrained Using Phase Equilibrium Modeling and Monazite Dating. *Minerals* **2022**, *12*, 1079. <https://doi.org/10.3390/min12091079>

Academic Editor: Bernhard Schulz

Received: 4 July 2022

Accepted: 23 August 2022

Published: 26 August 2022

**Publisher's Note:** MDPI stays neutral with regard to jurisdictional claims in published maps and institutional affiliations.



**Copyright:** © 2022 by the authors. Licensee MDPI, Basel, Switzerland. This article is an open access article distributed under the terms and conditions of the Creative Commons Attribution (CC BY) license (<https://creativecommons.org/licenses/by/4.0/>).

## 1. Introduction

Archean cratons are the stable remnants of the earth's early continents [1,2]. They preserve the oldest rocks and minerals, such as Hadean zircons of ages up to ~4.4 Ga in the Jack Hills of the Yilgarn Craton [3], Eoarchean rocks of  $\geq 3.8$  Ga in the Acasta Gneiss Complex of the Slave Craton [4,5], the Isua supracrustal belt of southwest Greenland [6], the Nuvvuagittuq Greenstone belt in northeast Canada [7] and the Eastern Block of the North China Craton (NCC) [8,9]. Some of the Archean cratons preserve the “dome-and-keel” structures, where the supracrustal rocks occur as rafts within tonalite–trondhjemite–granodiorite (TTG) domes, or as belts between them (e.g., the Superior Craton, Pilbara Craton, Kaapvaal Craton) [10–12]. These supracrustal rocks were subjected to greenschist- to granulite-facies or even ultra-high temperature (UHT) metamorphism [10]. Decoding their metamorphic evolution can provide insights into the tectonic regime of the early earth.

Archean supracrustal rocks in the NCC were subjected to metamorphism at the late Neoproterozoic (~2.50 Ga), being coeval with or shortly less than 50 Ma around the final pulse of the TTGs [13–15]. They were recovered to record different peak  $P$ – $T$  conditions. For example, the pelitic schist and amphibolites in the Taishan greenstone belt from the

western Shandong terrane underwent greenschist- to amphibolite-facies metamorphism with peak conditions of 3–6 kbar/350–600 °C defined using the conventional geothermobarometer [16]; the mafic granulites from the Miyun–Chengde terranes underwent an amphibolite- to granulite-facies metamorphism of 6.5–12.0 kbar/650–900 °C [17–19]; and the pelitic granulites from the East Hebei terrane preserve the typical UHT mineral assemblage of orthopyroxene, sillimanite and quartz, and were defined to have UHT peak conditions of 7–8 kbar/960–1040 °C using phase equilibrium modeling [20]. These supracrustal rocks share similar anticlockwise  $P$ – $T$  paths featured with post-peak near-isobaric cooling processes [21], which are normally recognized based on the symplektite around peak minerals, or the re-growth of hydrous minerals such as biotite and muscovite in metapelitic rocks or amphiboles in meta-basic rocks [16–20]. However, a garnet biotite gneiss of amphibolite facies from the East Hebei terrane was considered to record a different clockwise  $P$ – $T$  path based on the mineral compositions, especially the garnet zoning profiles [22]. Therefore, more studies need to be conducted on Archean supracrustal rocks to document their metamorphic paths, and to further address the Archean tectonic regime of the craton.

The Qingyuan area of the northern Liaoning terrane shows “dome-and-keel” structures, and have Archean supracrustal rocks occurring as enclaves within TTG domes. These supracrustal rocks were normally subjected to amphibolite- to granulite-facies metamorphism at the late Neoproterozoic (2.48–2.52 Ga) [23–29]. Wu et al. (2013) [30] and Wu and Wei (2021) [28] have developed detailed metamorphic studies on the meta-basic supracrustal rocks (garnet amphibolites) from Hongtoushan, Beisanjia and Douhutun, and proposed that they metamorphosed at conditions of 7.65–8.40 kbar/780–810 °C or ~10 kbar/870–890 °C with anticlockwise  $P$ – $T$  paths. Several models were proposed to be responsible for the metamorphic evolution of these amphibolites, and for the development of the Qingyuan area at the late Neoproterozoic, including: (i) a continental rift setting above a hotspot [31], (ii) a continent marginal arc setting triggered by oceanic subduction, followed by an arc–continent collision [24], (iii) a Neoproterozoic arc root setting [25], (iv) a primordial mantle plume setting [27,30] and (v) a vertical tectonic regime [28].

In this paper, we conduct detailed studies involving petrography, mineral chemistry, phase equilibrium modeling and monazite dating on biotite two-feldspar gneiss 15Q-4 collected from Hongtoushan of the Qingyuan area, to constrain its metamorphic evolution and to provide information for the tectonic regime.

## 2. Geological Setting

The North China Craton is composed of four Archean blocks, namely Yinshan, Ordos, Longgang and Langrim, and three Paleoproterozoic orogenic belts including the Khondalite belt, Jiao-Liao-Ji belt and Trans-North China Orogen [32] (Figure 1a). The Longgang and the Langrim blocks collided to form the Eastern Block through the ~1.90 Ga Jiao-Liao-Ji belt [33], while the Ordos and Yinshan blocks aggregated to form the Western Block along the Khondalite belt at ~1.95 Ga [34]. The Eastern and Western Blocks finally merged at 1.95–1.85 Ga by the Trans-North China Orogen [32,35]. Among them, the Longgang block is one of the oldest Archean blocks as it preserves the oldest rocks with ages up to ~3.85 Ga and detrital zircons of > 3.9 Ga in the East Hebei and northern Liaoning terranes [8,9,36].

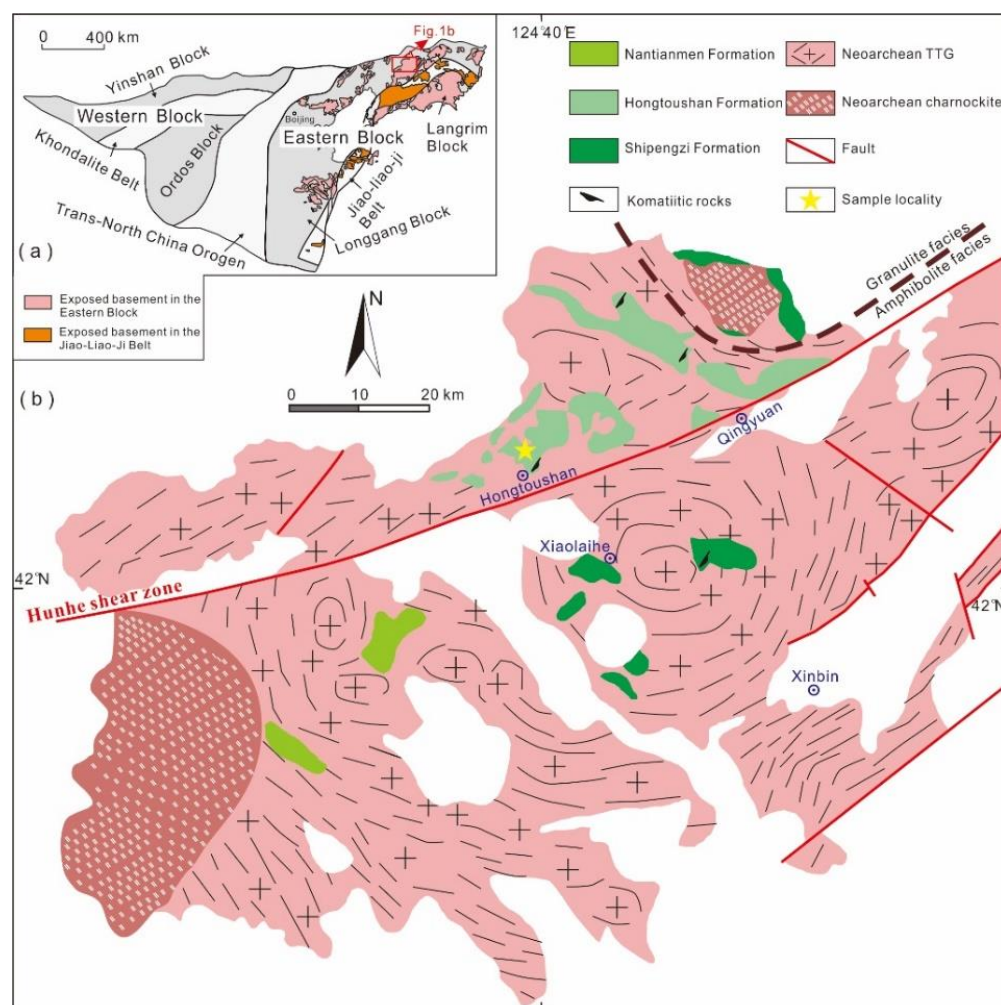


**Figure 1.** (a) Tectonic subdivision of the North China Craton (modified after [32,37]), showing the location of the Qingyuan area. (b) Geological sketch map of the Qingyuan area (modified after [25,27]), showing lithological distribution and sampling location.

The Qingyuan area from the northern Liaoning terrane shows domal structures of various scales, being composed of >80 % TTG gneisses and supracrustal rocks [30] (Figure 1b). The TTG gneisses were dated to share similar magmatic ages of 2.50–2.56 Ga [23–25,38]. The supracrustal rocks are known as the Qingyuan Group, occurring as various scales of rafts or enclaves within the TTG gneiss domes [25,39]. They are normally subdivided into Shipengzi, Hongtoushan and Nantianmen Formations upwards, constructing the typical sequence of greenstone belts [31]. The Shipengzi Formation is mainly composed of amphibolite and pyroxene amphibolite, with minor biotite plagioclase gneiss and ultramafic rocks including serpentinized dunite and lherzolite [25]. The Hongtoushan Formation, lying conformably on the Shipengzi Formation, mainly consists of pyroxene-absent or -bearing amphibolite and biotite plagioclase gneiss, with minor sillimanite- and/or kyanite-bearing gneiss. These rocks may have corresponding precursor rocks of tholeiitic basalt, siliciclastic rock and minor pelite. The Nantianmen Formation is predominated by amphibolite, two-mica quartz schist, biotite plagioclase gneiss, magnetite quartzite and marble, derived from basic volcanics, sediments, tuff and carbonate [25,27,31]. These supracrustal rocks underwent amphibolite- to granulite-facies metamorphism at the late Neoproterozoic [23–29], although a later Paleoproterozoic overprinting metamorphism of ~1.85 Ga was registered in meta-basic dykes in the area [28,40].

### 3. Petrology

#### 3.1. Petrography and Mineral Compositions

Minerals in this sample were analyzed using an electron microprobe analyzer (EPM; JXA-8100, JEOL, Tokyo, Japan) at the Laboratory of Orogenic Belt and Crustal Evolution of Peking University, China. The analyses were conducted under conditions of a 15 kV accelerating voltage and a 10 nA probe current with a beam diameter of 2  $\mu\text{m}$  for all phases. The results were standardized using natural and synthetic minerals of the SPI Company. Representative mineral compositions are listed in Table 1.

**Table 1.** Selected microprobe analyses for sample 15Q-4.

Mineral	Grt-c	Grt-r	Pl-c	Pl-m	Pl-r	Kfs	Bt
SiO <sub>2</sub>	36.86	36.95	62.41	62.22	62.50	65.18	35.74
TiO <sub>2</sub>	0.02	0.11	–	–	–	–	3.81
Al <sub>2</sub> O <sub>3</sub>	20.74	20.56	23.79	23.78	23.90	18.55	18.62
Cr <sub>2</sub> O <sub>3</sub>	–	0.02	–	–	–	–	0.03
FeO	32.71	34.50	–	0.09	0.24	–	20.27
MnO	3.12	3.83	0.04	–	0.04	0.03	0.14
MgO	4.77	2.68	–	–	–	–	8.66
CaO	0.86	1.11	5.15	5.52	5.42	0.03	0.02
Na <sub>2</sub> O	–	–	8.69	8.44	8.46	0.49	0.09
K <sub>2</sub> O	–	–	0.15	0.13	0.08	15.65	10.02
Total	99.08	99.78	100.21	100.20	100.65	99.95	97.49
O	12	12	8	8	8	8	11
Si	2.968	2.999	2.759	2.753	2.752	3.002	2.681
Ti	–	0.007	–	–	–	–	0.215
Al	1.969	1.967	1.240	1.240	1.241	1.007	1.646
Cr	–	–	–	–	–	–	0.002
Fe <sup>3+</sup>	0.093	0.022	–	0.003	0.009	–	–
Fe <sup>2+</sup>	2.110	2.319	–	–	–	–	1.272
Mn	0.213	0.263	–	–	–	–	0.009
Mg	0.572	0.324	–	–	–	–	0.968
Ca	0.074	0.097	0.244	0.262	0.256	–	0.002
Na	–	–	0.745	0.724	0.722	0.044	0.013
K	–	–	0.008	0.007	0.004	0.920	0.960
Sum	8.000	8.000	4.998	4.990	4.986	4.976	7.767
X(phase)	0.19	0.11	0.24	0.26	0.26	0.95	0.43
Y(phase)	0.025	0.032	0.75	0.73	0.74	0.05	–

$X(\text{Grt}) = X_{\text{Py}}$ ;  $Y(\text{Grt}) = X_{\text{Grs}}$ ;  $X(\text{Pl}) = X_{\text{An}}$ ;  $X(\text{Kfs}) = X_{\text{Or}}$ ;  $Y(\text{Pl}) = Y(\text{Kfs}) = X_{\text{Ab}}$ ;  $X(\text{Bt}) = X_{\text{Mg}}$ ; -c, grain core; -m, grain mantle; -r, grain rim. “–” means that the content is below the detection limit. The mineral formulas were calculated with the program AX (TJBH pages (filedn.com); accessed at 10 May 2022).

Sample 15Q-4 is a biotite two-feldspar gneiss, showing a gneissic structure and comprising 1–4 mm thick plagioclase-rich and -poor layers (Figure 2a). It is mostly composed of quartz (~40 vol.%), plagioclase (~25 vol.%), potassic feldspar (~25 vol.%), biotite (~5 vol.%), garnet (2 vol.%) and minor amounts of sillimanite, muscovite, magnetite and ilmenite. Garnet occurs as relict crystals of 0.3–0.7 mm with embayed rims in the plagioclase-poor layer (Figure 2a,b). It is departed by tiny-grained quartz, plagioclase, potassic feldspar and muscovite from fine-grained feldspars, showing features of melt recrystallization (Figure 2b). Most of the garnet grains have no zoning profiles with flat  $X_{\text{Py}}$  [=Mg/(Fe<sup>2+</sup>+Mg+Ca+Mn)], defined accordingly for other components of 0.19–0.23,  $X_{\text{Alm}}$  of 0.68–0.71,  $X_{\text{Grs}}$  of 0.027–0.035 (with an average of ~0.03) and  $X_{\text{Sps}}$  of 0.06–0.08 (Figure 3a), except one of them exhibiting a core→rim zoning pattern with significantly increasing  $X_{\text{Alm}}$  from ~0.71 to 0.74–0.77 and decreasing  $X_{\text{Py}}$  from ~0.19 to 0.11–0.15, and slightly increasing  $X_{\text{Grs}}$  from 0.025 to 0.035 (Figure 3b). Potassic feldspar normally occurs as tabular to anhedral grains of 0.1–0.8 mm coexisting with plagioclase, quartz and biotite (Figure 2a, b). It has  $X_{\text{Or}}$  [=K/(K+Na+Ca)] of 0.88–0.96 and  $X_{\text{Ab}}$  [=Na/(K+Na+Ca)] of 0.03–0.11. Some of them are perthite with albite lamellae. Potassic feldspar can also occur as irregular grains of <0.1 mm with tiny-grained plagioclase and quartz around garnet (Figure 2b). Plagioclase is mostly irregular grains of 0.1–0.3 mm (Figure 2a,b) and exhibits an outwards increase in  $X_{\text{An}}$  [=Ca/(K+Na+Ca)] from 0.22–0.24 to 0.25–0.27, sometimes with a slight decrease in the rim

(Figure 3c). It can also show as tiny grains of <0.1 mm around garnet. *Biotite* occurs as oriented flakes of 0.05–0.5 mm, forming the gneissic structure (Figure 2a). It exhibits a Ti of 0.19–0.22 p.f.u.,  $X_{Mg}$  [=Mg/(Mg+Fe<sup>2+</sup>)] of 0.42–0.44 (Figure 3d) and a high F of 0.16–0.29 wt.%. *Quartz* is mostly irregular grains of 0.1–0.3 mm, forming triple junction textures with plagioclase and potassic feldspar (Figure 2a,b), or as rounded inclusions within garnet or feldspars. It can also occur as tiny grains of <0.05 mm around garnet, or as irregular stripes with small dihedral angles at the margin of biotite and feldspars, showing features of melt crystallization. *Sillimanite* is normally acicular grains of 0.1–0.3 mm long, having a consistent orientation with biotite (Figure 2a,c). *Muscovite* shows as flakes of <0.1 mm, normally with sillimanite, around magnetite or at the rim of biotite (Figure 2c–g). *Ilmenite* only occurs as tiny grains included in biotite or potassic feldspar. *Magnetite* is irregular or rounded grains of 0.1–0.5 mm, normally surrounded by muscovite (Figure 2d–g). Based on the observations and mineral compositions presented above, the peak and final assemblages can be inferred. The peak assemblage consists of coexisting minerals including fine-grained garnet, plagioclase, potassic feldspar, biotite, sillimanite, quartz, magnetite and ilmenite, while the final assemblage is characterized by the presence of muscovite and the growth of tiny-grained quartz, plagioclase and potassic feldspar around garnet. It is worthy to mention that the final minerals occur locally around garnet, magnetite and biotite, showing potential melt accumulation.

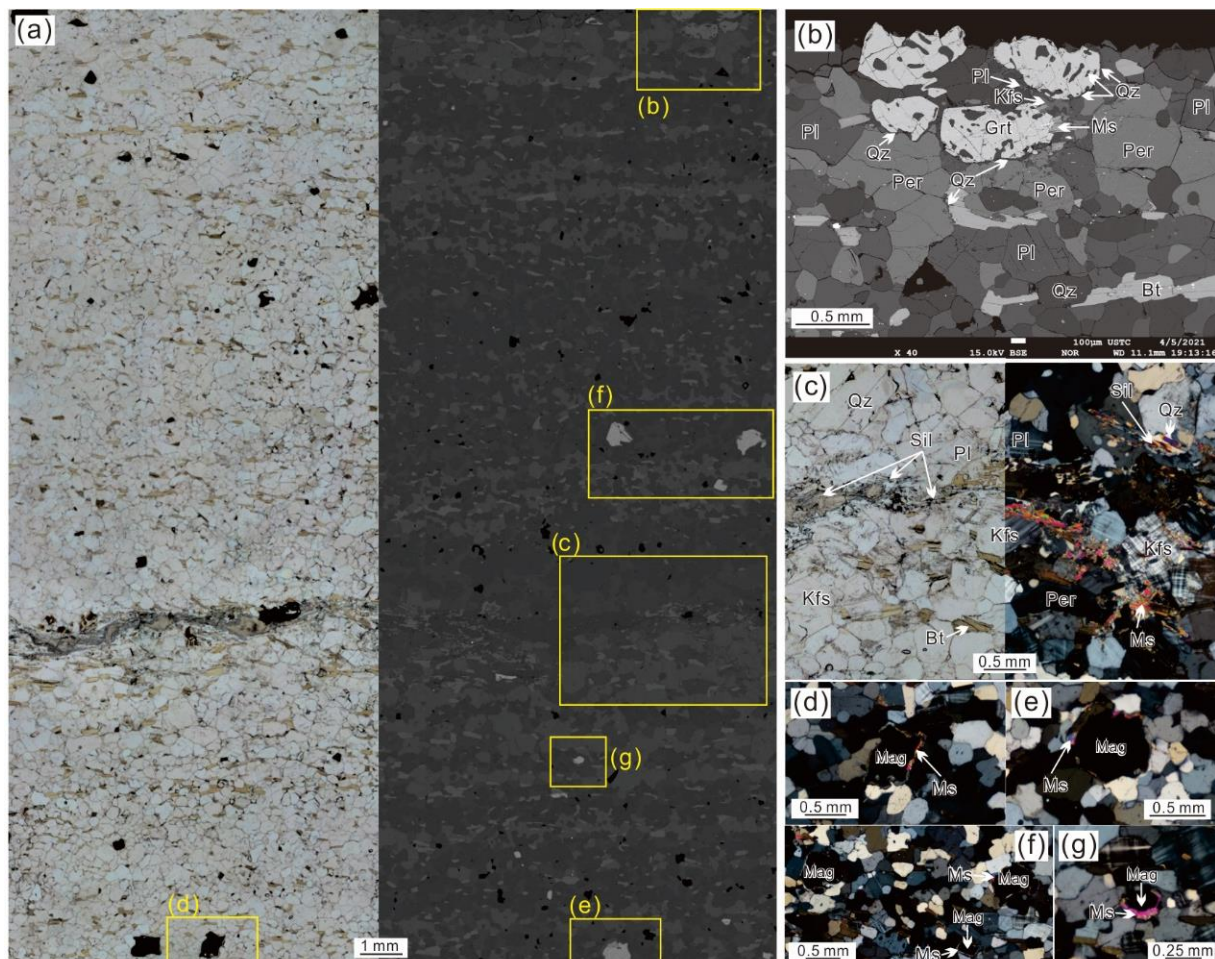


**Figure 2.** (a) Photomicrographs of the biotite two-feldspar gneiss using plane-polarized light (left) and back-scattered electron (right), showing the gneiss structure and compositional layers. (b) Garnet with embayed rims occurring in plagioclase-poor layer, and surrounded by tiny-grained feldspars, quartz and muscovite. (c) Sillimanite occurring in orientation with biotite. (d–g) Muscovite occurring around magnetite or biotite, suggesting melt crystallization.

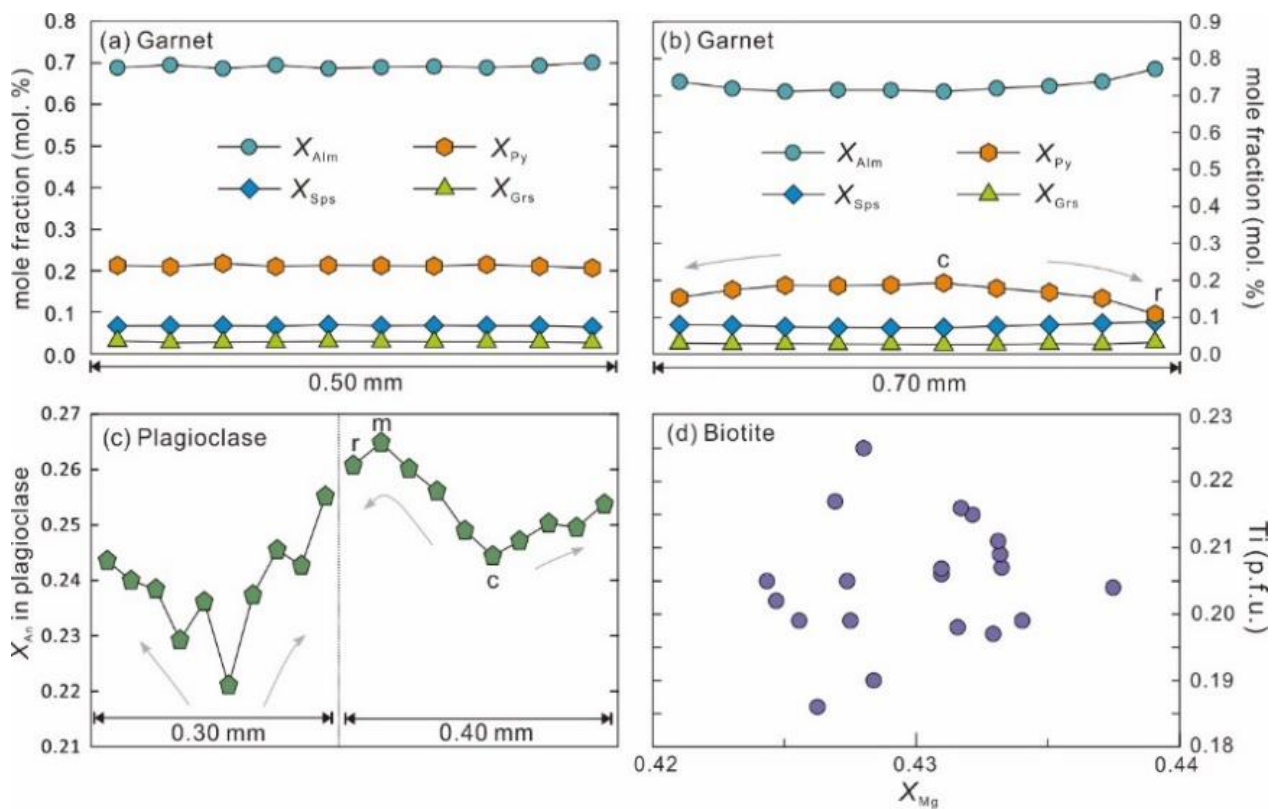


**Figure 3.** (a,b) Composition zoning profiles for garnets. (c)  $X_{An}$  profiles of plagioclases. (d)  $X_{Mg}$  versus Ti diagram showing the compositions of biotite.  $X_{Alm}$  [=Fe<sup>2+</sup>/(Fe<sub>2+</sub>+Mg+Ca+Mn)], defined accordingly for  $X_{Py}$ ,  $X_{Grs}$  and  $X_{Sps}$ ;  $X_{An}$  = Ca/(Ca+Na+K);  $X_{Mg}$  = Mg/(Mg+Fe<sup>2+</sup>).

### 3.2. Bulk-Rock Composition

The bulk-rock composition of the sample was analyzed at the Key Laboratory of Crustal Dynamics, Institute of Crustal Dynamics, CEA, Beijing, China, with X-ray fluorescence spectrometry (XRF) (Shimadzu, Kyoto, Japan). Analytical uncertainties were 1–3% for major elements. The sample had SiO<sub>2</sub> = 73.90 wt.%, TiO<sub>2</sub> = 0.21 wt.%, Al<sub>2</sub>O<sub>3</sub> = 12.70 wt.%, FeO<sub>tot</sub> = 3.88 wt.%, MgO = 0.66 wt.%, CaO = 1.36 wt.%, Na<sub>2</sub>O = 2.31 wt.%, K<sub>2</sub>O = 4.53 wt.% and MnO = 0.04 wt.%, showing higher SiO<sub>2</sub> and K<sub>2</sub>O and lower MgO, Na<sub>2</sub>O and CaO than the average Archean graywackes [41], and being similar to arkose with 52 percentage normative feldspar [42]. The Mg<sup>#</sup> (=MgO/(MgO+FeO)) and A/CNK [=Al<sub>2</sub>O<sub>3</sub>/(CaO+Na<sub>2</sub>O+K<sub>2</sub>O)] of the sample were 0.23 and 1.14, respectively.

### 4. Phase Equilibrium Modeling

Pseudosections can show various equilibrium mineral assemblages in the  $P$ – $T$  space for a single composition, based on internally consistent thermodynamic datasets [43]. It may be contoured by the compositions and/or proportions of minerals, providing insights into metamorphic  $P$ – $T$  conditions or even evolution histories [28,30]. In the calculation, we generally use the whole-rock compositions analyzed by ICP-OES to model the phase equilibria observed in a thin section, in addition to the following cases including (i) the presence of zoned porphyroblasts, (ii) the heterogeneous accumulation of minerals or melt and (iii) the presence of retrograde metamorphic reactions [44]. In our sample, garnet occurred only in the plagioclase-poor layer, so we preferred to generate an effective composition to calculate the pseudosection by consuming plagioclase to be ~10 vol.% instead of ~25 vol.% in the whole thin section.

A pseudosection for the sample 15Q-4 was modeled in the system NCKFMASHTO (Na<sub>2</sub>O–CaO–K<sub>2</sub>O–FeO–MgO–Al<sub>2</sub>O<sub>3</sub>–SiO<sub>2</sub>–H<sub>2</sub>O–TiO<sub>2</sub>–Fe<sub>2</sub>O<sub>3</sub>) using THERMOCALC 3.40

with the internally consistent thermodynamic dataset ds62 [43]. The re-parameterized  $a-x$  models included garnet, biotite, orthopyroxene, cordierite and melt [45], plagioclase and potassic feldspar [46] and magnetite and ilmenite [47]. The H<sub>2</sub>O and O (Fe<sub>2</sub>O<sub>3</sub>) contents were adjusted using  $T-M$  (H<sub>2</sub>O) and  $T-M$  (O) diagrams (Figure S1). The composition used in the  $P-T$  diagram was H<sub>2</sub>O = 1.38 mol.%, SiO<sub>2</sub> = 79.50 mol.%, Al<sub>2</sub>O<sub>3</sub> = 8.05 wt.%, CaO = 0.61 mol.%, MgO = 1.05 mol.%, FeO = 3.49 mol.%, K<sub>2</sub>O = 3.11 mol.%, Na<sub>2</sub>O = 2.41 mol.%, TiO<sub>2</sub> = 0.17 mol.% and O = 0.23 wt.%, showing higher SiO<sub>2</sub>, Al<sub>2</sub>O<sub>3</sub> and K<sub>2</sub>O, and lower CaO than the analyzed whole-rock composition.

The  $P-T$  pseudosection was calculated with quartz, potassic feldspar and plagioclase in excess in the  $P-T$  window of 2–12 kbar/600–850 °C. The fluid-absent solidus occurred at temperatures of 660–760 °C. Garnet had a wide stability almost all over the window. The biotite-out curve was nearly temperature-dependent within temperatures of 750–790 °C. The pseudosection was contoured with isopleths of  $X_{Py}$  and  $X_{Grs}$  in garnet (xg and zg on Figure 4) and  $X_{Mg}$  and Ti in biotite (xb and tb on Figure 4) for the relevant mineral assemblages. The inferred peak mineral assemblage involving garnet, potassic feldspar, plagioclase, biotite, sillimanite, quartz, magnetite and ilmenite was stable in a large  $P-T$  range of 4–9 kbar/730–780 °C in the presence of melt, bounded by biotite- and ilmenite-out curves on the higher and lower temperature limits, and muscovite- and cordierite-in curves on the higher and lower pressure limits. The measured  $X_{Py}$  of 0.19–0.23 in the core of the garnet was plotted in this field and yielded a narrow peak temperature range of 750–775 °C, being consistent with the measured  $X_{Mg}$  of 0.42–0.44 in biotite. The temperature uncertainties of the  $X_{Py}$  and  $X_{Mg}$  isopleths were calculated to be ~0 °C and ~12 °C (two-sigma level), respectively, using THERMOCALC. These results are considered to be minimum because they are propagated from the uncertainties on the enthalpy alone. The predicted Ti in biotite that can be plotted in the field of peak mineral assemblage has a maximum of ~0.16 p.f.u., lower than the measured Ti of 0.19–0.22 p.f.u. in the biotite of the sample. The lower  $X_{Py}$  of 0.11–0.15 in the rim of the garnet matches this peak field and the ilmenite-absent field, defining a cooling temperature of 720–740 °C. The isopleths of  $X_{Grs}$  in the garnet are near-horizontal on Figure 4, exhibiting positive relationship with pressures. The measured  $X_{Grs}$  of 0.025–0.035 in the garnet yielded pressures of 5.5–7.7 kbar in the relevant field, and the average value of ~0.03 defined peak and cooling pressures of 7–6 kbar with an uncertainty of ~0.2 kbar (two-sigma level) at the constrained peak and cooling temperatures.

However, the observed final assemblage featured with the presence of muscovite occurred at higher pressures of >7.2 kbar, being inconsistent with the defined cooling path. This may be because the residual melts were locally segregated and crystallized to form the final assemblage, being not completely equilibrated with other minerals. Thus, a  $T-M$  (melt) pseudosection was calculated at ~6 kbar by adding more melts in the mineral assemblage on the solidus of Figure 4 to model the phase equilibrium of the final assemblage. As shown in Figure 5, the fluid-absent solidus shifted slightly when the mode of the melt increased, and the muscovite-present final assemblage occurred at ~700 °C on the solidus when the melt mode increased to >3 mol.%.

As a result, the core→rim decreasing  $X_{Py}$  from 0.19–0.23 to 0.11–0.15 at a constant  $X_{Grs}$  of ~0.03 in the garnet suggests a post-peak near-isobaric cooling path on the pseudosection from ~7 kbar/750–775 °C in the inferred peak mineral assemblage to ~6 kbar/720–740 °C in the ilmenite-absent assemblage. The muscovite-present final assemblage defines a final condition of ~6 kbar/~700 °C on the solidus. The metamorphic reaction along the path was calculated to be  $Grt + Ksp + Ilm + Mag + Liq = Pl + Bt + Sill + Qz + Ms$ , being responsible for the occurrence of tiny-grained feldspars, muscovite and quartz around the embayed garnet.



## 5. Monazite Age Dating

Monazite, a common accessory mineral in metamorphic and magmatic rocks or a detrital mineral in sedimentary rocks, normally has a low initial Pb and high Th, U and REE contents [49]. It grows or recrystallizes during amphibolite- to granulite-facies metamorphism and is prone to being partially to totally reset from isotope inheritance [50]. These make it more sensitive relative to zircon in recording metamorphic ages [51]. In this sample, monazites were normally anhedral to rounded grains of 50–150  $\mu\text{m}$  with length/width ratios of 1:1–3:1. They occurred in equilibrium with potassic feldspar, plagioclase and quartz, and could also have these minerals as inclusions, suggesting their metamorphic origins. The BSE imaging of individual monazite grains was carried out at the Nanjing Hongchuang Exploration Technology Service Company Limited on a HTACHI S-3000N scanning electron microscope (SEM) (Tokyo, Japan) with a 2 min scanning time at conditions of 15 kV and 120  $\mu\text{A}$ . The LA-ICP-MS isotope analyses were performed at the Wuhan Sample Solution Analytical Technology Co., Ltd., Wuhan, China, using an Agilent 7500a ICP-MS system connected with an excimer laser ablation system (GeoLas 2005) with an automatic positioning system. Detailed operating conditions and calibrating standards have been given by Liu et al. (2008b) [52].  $^{207}\text{Pb}/^{206}\text{Pb}$ ,  $^{206}\text{Pb}/^{238}\text{U}$  and  $^{207}\text{Pb}/^{235}\text{U}$  ratios and apparent ages were calculated using the ICPMS-DataCal 10.9 [53]. We used “Isoplot 3.0” to conduct the age calculations and the plotting of the concordia diagrams [54].

Forty analyses were undertaken on monazites, and the result is presented in Table 2. These analyses had apparent  $^{207}\text{Pb}/^{206}\text{Pb}$  ages ranging between  $2553 \pm 24$  Ma and  $2461 \pm 21$  Ma. All of them were plotted on or near the concordia curve, defining a common upper intersect age of  $2501 \pm 6$  Ma (MSWD = 1.2,  $n = 40$ ) and a weighted mean  $^{207}\text{Pb}/^{206}\text{Pb}$  age of  $2501 \pm 7$  Ma (MSWD = 0.83,  $n = 40$ ) (Figure 6a). These monazites exhibited right-inclined REE patterns with negative Eu anomalies ( $\text{Eu}/\text{Eu}^* = 0.06\text{--}0.48$ ) and a high  $(\text{Gd}/\text{Lu})_{\text{N}}$  of 55.71–215.89 (Figure 6b). They had a neglectable common Pb of 0–4 ppm and a total Pb of 767–3802 ppm. The Th/U ratios ranged within 1.3–68.3 with an average of 21.8 as the Th and U values were 3729.7–29,017.3 ppm and 306.3–3289.2 ppm, respectively (Figure 6c).

Table 2. Monazite isotopic data for sample 15Q-4.

Spot	Th (ppm)	U (ppm)	Th/U	Measured Isotopic Ratios						Corrected Ages (Ma)					
				$^{207}\text{Pb}/^{206}\text{Pb}$	1 $\sigma$	$^{207}\text{Pb}/^{235}\text{U}$	1 $\sigma$	$^{206}\text{Pb}/^{238}\text{U}$	1 $\sigma$	$^{207}\text{Pb}/^{206}\text{Pb}$	1 $\sigma$	$^{207}\text{Pb}/^{235}\text{U}$	1 $\sigma$	$^{206}\text{Pb}/^{238}\text{U}$	1 $\sigma$
15Q-4-01	4215	657	6.42	0.164	0.002	10.729	0.163	0.474	0.003	2498	24	2500	14	2501	14
15Q-4-02	15,507	665	23.30	0.163	0.002	10.691	0.152	0.477	0.003	2483	24	2497	13	2515	13
15Q-4-03	24,917	579	43.00	0.163	0.002	10.975	0.155	0.490	0.003	2484	24	2521	13	2569	15
15Q-4-04	13,857	524	26.43	0.164	0.002	10.551	0.145	0.468	0.003	2495	24	2484	13	2473	12
15Q-4-05	17,492	633	27.61	0.164	0.002	10.304	0.149	0.456	0.003	2494	23	2462	13	2422	12
15Q-4-06	12,521	335	37.34	0.161	0.003	10.528	0.183	0.475	0.003	2478	32	2482	16	2504	15
15Q-4-07	19,158	484	39.61	0.166	0.003	10.917	0.171	0.477	0.004	2518	27	2516	15	2515	16
15Q-4-08	9527	2243	4.25	0.164	0.002	10.660	0.123	0.471	0.002	2498	19	2494	11	2488	10
15Q-4-09	4853	477	10.17	0.166	0.002	10.992	0.163	0.482	0.003	2513	26	2522	14	2536	14
15Q-4-10	9960	2433	4.09	0.164	0.002	10.588	0.111	0.468	0.002	2496	17	2488	10	2476	10
15Q-4-11	13,921	651	21.38	0.166	0.003	10.649	0.150	0.466	0.003	2516	26	2493	13	2467	12
15Q-4-12	10,963	1184	9.26	0.166	0.002	10.654	0.138	0.467	0.003	2515	24	2493	12	2469	12
15Q-4-13	11,328	479	23.66	0.164	0.003	10.562	0.156	0.469	0.003	2494	21	2485	14	2479	14
15Q-4-14	13,058	896	14.57	0.162	0.002	10.491	0.145	0.468	0.003	2483	21	2479	13	2475	14
15Q-4-15	13,026	1342	9.70	0.163	0.002	10.682	0.116	0.475	0.002	2487	19	2496	10	2507	11
15Q-4-16	8487	2504	3.39	0.161	0.002	10.552	0.107	0.475	0.002	2478	17	2484	10	2504	10
15Q-4-17	21,469	1028	20.89	0.163	0.002	10.529	0.130	0.468	0.003	2487	21	2482	12	2476	12
15Q-4-18	29,017	895	32.41	0.162	0.002	10.583	0.148	0.472	0.003	2483	24	2487	13	2492	13
15Q-4-19	8749	2015	4.34	0.160	0.002	10.527	0.127	0.475	0.003	2461	21	2482	11	2507	12
15Q-4-20	13,411	2579	5.20	0.163	0.002	10.563	0.123	0.470	0.002	2487	14	2485	11	2481	10
15Q-4-21	6961	1106	6.29	0.163	0.002	10.606	0.139	0.473	0.003	2484	22	2489	12	2495	12
15Q-4-22	14,278	547	26.09	0.163	0.003	10.767	0.174	0.480	0.004	2482	26	2503	15	2528	16
15Q-4-23	20,755	354	58.62	0.164	0.003	10.892	0.209	0.483	0.004	2494	31	2514	18	2539	18
15Q-4-24	7409	2754	2.69	0.164	0.003	10.655	0.178	0.472	0.003	2494	28	2494	16	2492	13
15Q-4-25	18,834	478	39.37	0.164	0.003	10.790	0.201	0.477	0.004	2502	66	2505	17	2513	16
15Q-4-26	13,800	610	22.62	0.166	0.003	11.011	0.190	0.482	0.004	2513	27	2524	16	2534	16
15Q-4-27	22,458	437	51.41	0.168	0.003	11.130	0.171	0.482	0.004	2535	27	2534	14	2535	15
15Q-4-28	19,744	702	28.13	0.166	0.002	10.942	0.159	0.477	0.003	2524	24	2518	14	2513	15
15Q-4-29	16,941	896	18.90	0.169	0.002	10.843	0.143	0.466	0.003	2545	22	2510	12	2464	12
15Q-4-30	4372	3289	1.33	0.167	0.002	10.879	0.139	0.471	0.003	2531	22	2513	12	2487	12
15Q-4-31	20,928	306	68.34	0.169	0.003	11.068	0.196	0.474	0.004	2552	31	2529	17	2503	18
15Q-4-32	3730	653	5.71	0.170	0.002	11.323	0.166	0.484	0.003	2553	24	2550	14	2545	15
15Q-4-33	11,496	402	28.62	0.167	0.003	10.977	0.193	0.475	0.004	2532	29	2521	16	2507	17
15Q-4-34	12,076	683	17.68	0.165	0.002	10.550	0.147	0.464	0.003	2506	24	2484	13	2458	12
15Q-4-35	20,761	750	27.67	0.165	0.002	10.786	0.157	0.473	0.003	2509	58	2505	14	2498	13
15Q-4-36	21,990	912	24.11	0.167	0.003	10.778	0.164	0.469	0.003	2524	26	2504	14	2478	12
15Q-4-37	7265	2277	3.19	0.163	0.002	10.824	0.148	0.480	0.003	2500	24	2508	13	2529	11
15Q-4-38	10,694	2297	4.66	0.165	0.002	10.750	0.148	0.473	0.003	2506	23	2502	13	2496	12
15Q-4-39	19,216	572	33.58	0.167	0.003	11.077	0.171	0.481	0.004	2529	27	2530	14	2532	16
15Q-4-40	18,429	539	34.16	0.165	0.003	11.005	0.195	0.483	0.004	2511	31	2524	17	2541	17

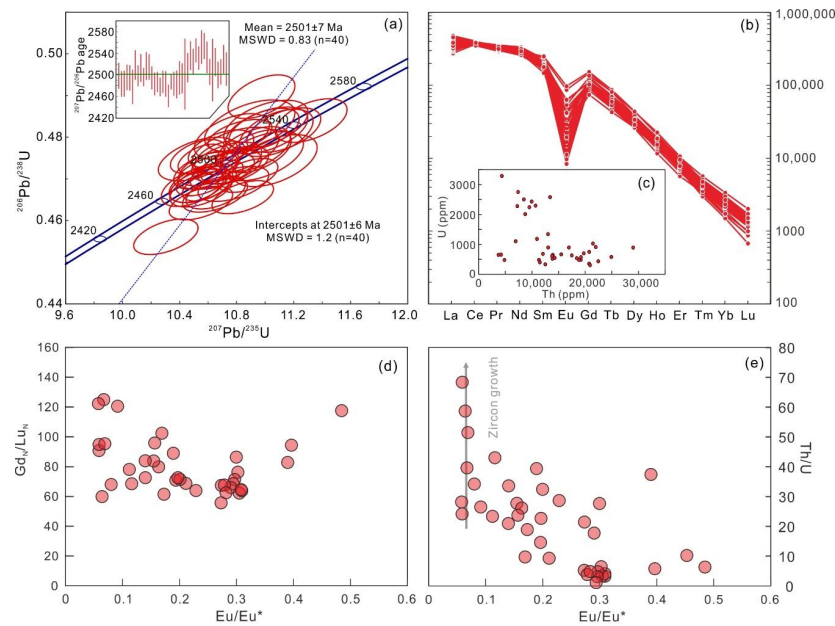


**Figure 6.** (a) U–Pb isotopic age distribution and average of analyzed monazites. (b) Chondrite-normalized REE patterns for the monazites (normalizing values after [55]). (c) Th versus U diagram for the monazites. (d,e) Eu/Eu\* versus (Gd/Lu)<sub>N</sub> and Th/U diagrams for the monazites.

## 6. Discussion

### 6.1. Metamorphic Evolution

The biotite two-feldspar gneiss 15Q-4 was recovered to record a post-peak near-isobaric cooling process from the peak. The peak temperature was constrained to be 750–775 °C based on the stability of the inferred peak mineral assemblage (Grt + Kfs + Pl + Bt + Sil + Qz + Mag + Ilm + Liq) on the pseudosection, together with mineral compositions including the  $X_{Py}$  of 0.19–0.23 in the garnet core and  $X_{Mg}$  of 0.42–0.44 in biotite. However, the measured Ti of 0.19–0.22 in biotite cannot be plotted in the peak field. This may be because the biotite-out curve was underestimated in the modeling. The predicted biotite-present fields on the pseudosection occupied temperatures of <790 °C (Figure 4), significantly lower than the results from experimental work where the biotite can be stable to >900 °C at ~7 kbar in pelites and greywackes [56]. It would be enlarged to higher temperatures if one modified the thermodynamic model by changing the ordering of Ti onto the M2 octahedral site instead of the M1 site [57], or incorporating other components (i.e., fluorine) in the system [58]. Thus, it is also possible that the measured Ti of 0.19–0.22 in biotite may suggest a higher peak temperature of >790 °C. A cooling temperature of 720–740 °C was constrained in the peak field or the ilmenite-absent field by the  $X_{Py}$  of 0.11–0.5 in the garnet rim, while a final temperature of ~700 °C was defined by the stability of the muscovite-present final assemblage. This is consistent with the experimentally constrained temperature for the reaction of  $Ms + Ab + Qz = Sil + Kfs + Liq$  in Petö (1976) [59]. The pressure was constrained to be within 6–7 kbar by the average  $X_{Grs}$  value of ~0.03 in the garnet core and rim in the relevant assemblages. Therefore, the post-peak near-isobaric cooling process to the final condition was correspondingly suggested by the core→rim decreasing  $X_{Py}$  at a constant  $X_{Grs}$  in the garnet, supported by the mineral relations that the tiny-grained feldspars, muscovite and quartz were around the embayed garnet. Furthermore, we prefer to consider that the sample was subjected to an anticlockwise metamorphic evolution involving a pre-peak up-pressure process based on the following reasons: (i) there was a slight core→rim increasing trend in the  $X_{Grs}$  of garnet, suggesting an up-pressure process on the pseudosection (Figure 4); and (ii) the interlaid garnet amphibolite in the same locality was proposed to record a pre-peak low- $P$ - $T$  mineral assemblage within garnet [28,30].

For comparison, the peak condition was estimated using the garnet–biotite (GB) geothermometer [60], and the garnet–biotite–plagioclase–quartz (GBPQ) geobarometer [61]. The garnet core with a maximum  $X_{Py}$ , the biotite with a maximum  $X_{Mg}$  and Ti and a plagioclase

with a maximum  $X_{An}$  were used in the calculation. The peak temperature was calculated to be  $751 \pm 25$  °C, which is consistent with the calculated result ( $\sim 705$  °C) using a Ti-in-biotite geothermometer within an error of  $\pm 50$  °C [62], and also the defined peak temperature using a pseudosection. However, the calculated pressure of  $3.7 \pm 1.0$  kbar was lower than the constrained pressure on the pseudosection using the  $X_{Grs}$  of the garnet. This may be because the plagioclase composition used in the calculation was inappropriate. Possible reasons may be: (i) the plagioclase may not have reached complete equilibrium with the garnet during metamorphism as they rarely contacted each other; or (ii) compositional changes in the plagioclase were small and hard to be analyzed when there were too many plagioclases equilibrated with garnet, just as Spear and Florence (1992) [63] pointed out. Therefore, we favor the constrained pressure by the pseudosection.

The metamorphic age was dated to be  $\sim 2.50$  Ga by the monazite, and is preferable to be interpreted as the age at the post-peak cooling process because (i) the  $(Gd/Lu)_N$  values showed a neglectable correlation with  $Eu/Eu^*$  (Figure 6d), suggesting that the monazite was not correlated with the garnet growth in the pre-peak process; and (ii) the Th/U ratios had a significant increase at an  $Eu/Eu^*$  of  $< 0.1$  (Figure 6e), indicating that monazite may crystallize with zircon from the melt in the cooling process [51].

## 6.2. Tectonic Implications

Sample 15Q-4 was recovered to have an anticlockwise  $P$ – $T$  path, involving a peak temperature of  $750$ – $775$  °C or even  $> 790$  °C at  $\sim 7$  kbar, and a subsequent cooling process to  $\sim 700$  °C at  $\sim 6$  kbar on the solidus. Similar metamorphic paths were proposed in meta-basaltic rocks from Qingyuan areas [28,30] and in supracrustal rocks including mafic, pelitic or greywacke rocks in other Archean terranes in the Eastern Block of the NCC, especially the East Hebei terrane [20,44] (Figure 7), although the metamorphic  $P$ – $T$  conditions range from amphibolite-facies to normal or even ultra-high temperature granulite-facies. These metamorphic processes were all dated to occur at  $\sim 2.50$  Ga [20,28,30], being coeval with the final pulse of the crystallization ages of the TTGs [14].

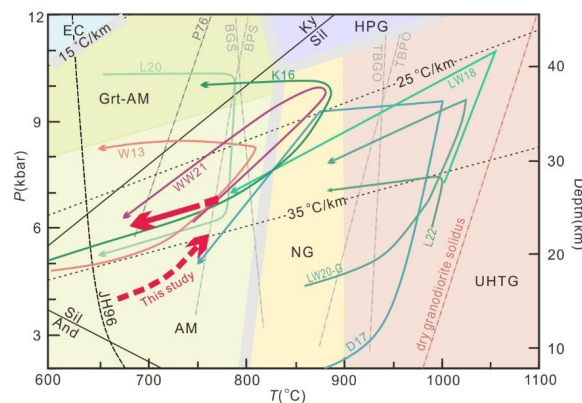


**Figure 7.** Summarized  $P$ – $T$  conditions and paths for Neoproterozoic supracrustal rocks from the Qingyuan area, and their comparison with the metamorphic paths of supracrustal rocks from the East Hebei Terrane. Thick arrow represents the  $P$ – $T$  path of the studied sample 15Q-4. The  $P$ – $T$  paths from the Qingyuan area: W13, from [30] and WW21, from [28]. The  $P$ – $T$  paths from the East Hebei terrane: D17, from [44]; K16, from [64]; LW18, from [65]; L20, from [22]; LW20-G, from meta-greywacke in [66]; L22, from [20]. BGS and BPS, and TBGO and TBPO are experimentally constrained biotite-in and -out lines for greywacke and pelite compositions from [56]. JH96—the  $H_2O$ -saturated granite solidus in the system  $Qz$ – $Ab$ – $Or$ – $H_2O$  [67]; P76—experimentally constrained  $Ms + Ab + Qz = Sil + Kfs + Liq$  reaction from [59]. The dry solidus of granodiorite is from [68]. The reactions of  $Al_2SiO_5$  are calculated by THERMOCALC. The distributions of metamorphic facies are from [69] and abbreviations are: HPG, high- $P$  granulite facies; NG, ‘normal’ granulite facies; UHTG, ultra-high temperature granulite facies; AM, amphibolite facies; Grt-AM, garnet amphibolite facies; EC, eclogite facies.

Metamorphic  $P$ – $T$  paths are of great significance in inferring the tectonic settings and processes [70]. Anticlockwise  $P$ – $T$  paths involving post-peak near-isobaric cooling are normally considered to be related with the intrusion or underplating of mantle-derived magma [15,71,72]. In the Qingyuan area of the northern Liaoning terrane, these anticlockwise metamorphic paths are argued to result from (i) a continental rift above a hotspot [31], (ii) a continent marginal arc setting triggered by oceanic subduction [24], (iii) a Neoproterozoic arc root setting [25], (iv) a (primordial) mantle plume setting [27,30,73] and (v) a vertical sagduction regime [28]. Among these models, the arc-correlated geological settings were normally based on the arc-like geochemical compositions of the basalts, while the rift model was mostly from the bimodal volcanic assemblages in the terrane or even in the whole NCC. However, they cannot be responsible for the geological features including (i) the Archean unique “dome-and-keel” structures in the terrane, which are inconsistent with the linear structures formed in modern plate tectonics, but are successfully modeled in the Archean vertical tectonic regime [74], (ii) the occurrence of (basaltic) komatiite, which suggests an extremely high mantle potential temperature of  $>1650$  °C [25,31] and (iii) the synchronicity among the deposition and metamorphism of supracrustal rocks, the magmatism of the TTGs and the metallogenesis of sulfide Cu-ore deposits within ~50 Ma around ~2.5 Ga [14,37] (Table 3). Therefore, we follow Wu and Wei (2021) [28] to consider that the anticlockwise metamorphic paths of the supracrustal rocks may be subjected to a vertical tectonic process, where the upwelling of the TTG magma occurs with the down dropping of supracrustal rocks. This may be triggered or correlated with Archean mantle plume.

**Table 3.** Summary of metamorphic ages of supracrustal rocks and magmatic ages of TTGs in the Qingyuan area.

Rocks	Location	Magmatic Age (Ma)	Metamorphic Age (Ma)	Method	Reference
Granitic gneiss	Hongtoushan	2520 ± 16		Conventional multi-grain	Li and Shen, 2000 [75]
Granitic gneiss	Paozigou	2519 ± 77		SHRIMP	Wan et al., 2005 [23]
Amphibole fine-grained gneiss	Xiaolaihe	2515 ± 6			
Amphibole fine-grained gneiss	Tangtu	2515 ± 7			
Amphibole fine-grained gneiss	Qingyuan	2494 ± 5	2479 ± 5		
TTG gneiss	Fushun	2530 ± 22	2477 ± 13		
TTG gneiss	Xiaolaihe	2556 ± 18	2469 ± 19		
Quartz dioritic gneiss	Majuanzi	2571 ± 7		LA-ICP-MS	
Quartz diorite	Tangtu	2496 ± 18	2427 ± 49		
Plagioclase amphibolite	Tangtu	2530 ± 5	2507 ± 11; 2461 ± 26; 2350 ± 26		Bai et al., 2014 [76]
Tonalitic gneiss	Jiubingtai	2544 ± 4			
Trondhjemitic gneiss	Tangtu	2518 ± 23	2473 ± 30		
Trondhjemitic gneiss	Jiubingtai	2550 ± 10	2508 ± 49		
Syenitic granite	Jiubingtai	2522 ± 4			
Quartz diorite	Yangjiadian		2478 ± 18	LA-ICP-MS	
Tonalite	Binghugou	2528 ± 6			Peng et al., 2015 [25]
	Binghugou	2520 ± 12			
Quartz mozodiorite	Yangjiadian	2504 ± 5			
Amphibolite	Pinglinghou		2474 ± 5		
Granulite	Jingjiagou	2537 ± 8	2482 ± 5	SHRIMP	
Grt-Hb-Bt-Pl gneiss	Longwangmiao	2555 ± 10	2476 ± 9		Wu et al., 2016 [26]
Grt-Bt-Pl gneiss	Xiaolaihe	2497 ± 4	2476 ± 10		
Granulite	Pinglinghou	2515 ± 39	2485 ± 3		
Grt-amphibolite	Tangtu		2489 ± 3		
Grt-Bt-Pl gneiss	Tongshi		2484 ± 14		
Trondhjemitic gneiss	Xiajiabao	2559 ± 11		LA-ICP-MS	
Trondhjemitic gneiss	Huangqizhai	2558 ± 11			Wang et al., 2016 [77]
Tonalitic gneiss	Xiajiabao	2525 ± 6	2496 ± 6		
Trondhjemitic gneiss	Dasuhe	2504 ± 14			
Monogranitic gneiss	Xiaojinchang	2529 ± 3	2495 ± 38		
Monogranitic gneiss	Hongqizhai	2515 ± 3			
Tonalitic gneiss	Jiubingtai	2522 ± 8		LA-ICP-MS	
Tonalitic gneiss	Jiubingtai	2511 ± 4	2484 ± 6		Wang et al., 2016 [78]
Biotite trondhjemitic gneiss	Hongmiaozhi	2528 ± 9			
Trondhjemitic gneiss	Yongling	2537 ± 9	2487 ± 5		
Tonalitic gneiss	Sandaoguan	2524 ± 6			

Table 3. Cont.

Rocks	Location	Magmatic Age (Ma)	Metamorphic Age (Ma)	Method	Reference
Hornblende plagioclase gneiss	Tangtu	2550 ± 18	2508 ± 10	LA-ICP-MS	
Hornblende plagioclase gneiss		2561 ± 5			
Amphibolite	Weiziyu	2757 ± 6			
Amphibolite	Huiyuan	2525 ± 16			
TTG gneiss	Hongmiaozi	2592 ± 4	2532 ± 43		
TTG gneiss	Hongmiaozi	2585 ± 6			
TTG gneiss	Hongtoushan	2573 ± 4			
TTG gneiss	Baiqizhai	2558 ± 4			Wang et al., 2017 [79]
TTG gneiss	Huiyuan	2541 ± 5			
TTG gneiss	Huiyuan	2537 ± 5			
Potassic granitoid gneiss	Qingyuan	2554 ± 23	2497 ± 19; 2495 ± 21		
Potassic granitoid gneiss	Baiqizhai	2554 ± 17			
Potassic granitoid gneiss	Huiyuan	2546 ± 3			
Potassic granitoid gneiss	Hongtoushan	2515 ± 3			
Porphyritic granodiorite	Yingerbu	2559 ± 7	2500 ± 6	LA-ICP-MS	
Porphyritic granodiorite	Majuanzi	2550 ± 4	2510 ± 5		
Porphyritic granodiorite	Fushun	2542 ± 4			
Medium-grained granodiorite	Weiziyu	2545 ± 12			Wang et al., 2017 [39]
Medium-grained monzogranite	Yongling	2550 ± 8	2515 ± 9		
Porphyritic quartz syenitic gneiss	Shiwen	2505 ± 9			
Amphibolite	Xiaolaihe	2530 ± 4		LA-ICP-MS	
Amphibolite	Hongtoushan	2539 ± 7			
Amphibolite	Tangtu	2501 ± 5			
Amphibolite	Fangniugou	2516 ± 3			Li and Wei, 2017 [27]
Amphibolite	Fangniugou	2520 ± 4	2495 ± 8		
Amphibolite	Jinfengling	2547 ± 19	2486 ± 37		
Trondhjemitic gneiss	Hongmiaozi	2585 ± 14		LA-ICP-MS	
Tonalitic gneiss	Majuanzi	2588 ± 12			Wang et al., 2018 [80]
Monogranitic gneiss	Weiziyu	2555 ± 4	2516 ± 12		
Biotite plagioclase gneisses	Xiaolaihe	2565 ± 8	2516 ± 7	LA-ICP-MS	Peng et al., 2019 [81]
Mafic granulite	Dongjinggou		1938 ± 12; 1843 ± 10	LA-ICP-MS	Duan et al., 2019 [40]
Garnet amphibolite	Lvjiapu		2502 ± 9	LA-ICP-MS	
Garnet amphibolite	Majiadian		1821 ± 9		Wu and Wei, 2021 [28]
Dioritic gneiss	Qingyuan	2519 ± 13	2457 ± 21; 2389 ± 20	LA-ICP-MS	
Tonalitic gneiss	Qingyuan	2556 ± 4	2496 ± 8		
Trondhjemitic gneiss	Qingyuan	2542 ± 5	2495 ± 7		Li et al., 2021 [82]
Trondhjemitic gneiss	Qingyuan	2506 ± 8	2453 ± 13; 2401 ± 12		
Biotite two-feldspar gneiss	Hongtoushan		2473 ± 16	LA-ICP-MS	Li et al., 2022 [29]
Biotite two-feldspar gneiss	Hongtoushan		2501 ± 7	LA-ICP-MS	this paper

## 7. Conclusions

(1) The biotite two-feldspar gneiss from the Hongtoushan of the Qingyuan area, the NCC, were limited to have a peak condition of 750–775 °C, ~7 kbar, together with a post-peak near-isobaric cooling process to a final condition of ~700 °C, ~6 kbar.

(2) Monazite dating yielded a metamorphic age of ~2.50 Ga for the sample, coeval with the final magmatism of the TTGs in the terrane.

(3) We prefer a vertical sagduction process to be responsible for the metamorphic evolution of the Qingyuan area. This process may be correlated with Archean mantle plume.

**Supplementary Materials:** The following figure is available online at <https://www.mdpi.com/article/10.3390/min12091079/s1>. Figure S1: *T-M*(H<sub>2</sub>O) and *T-M*(O) diagrams at 6.5 kbar.

**Author Contributions:** T.L. calculated the pseudosection, performed the data analyses and wrote the manuscript. Z.L. collected the samples, conducted the experiments, developed the project and revised the manuscript. C.W. revised the manuscript. All authors discussed the results and were involved in writing and revising the paper. All authors have read and agreed to the published version of the manuscript.

**Funding:** This work was financially supported by the Science Foundation of China University of Petroleum, Beijing (Grant Number: 2462021YXZZ004) and the National Natural Science Foundation of China (Grant Numbers: 42002238 and 41872057).

**Acknowledgments:** The authors thank assistant editor and managing editor very much for their editorial work, and two anonymous reviewers for their constructive and insightful comments and suggestions.

**Conflicts of Interest:** The authors declare that the research was conducted in the absence of any commercial or financial relationships that could be construed as a potential conflict of interest.

## References

1. James, D.E.; Fouch, M.J. Formation and evolution of Archean cratons: Insights from southern Africa. In *The Early Earth: Physical, Chemical and Biological Development*; Fowler, C.M.R., Ed.; Geological Society London Special Publications: Bath, UK, 2002; pp. 1–26.
2. King, S.D. Archean cratons and mantle dynamics. *Earth Planet. Sci. Lett.* **2005**, *234*, 1–14. [[CrossRef](#)]
3. Wilde, S.A.; Valley, J.W.; Peck, W.H.; Graham, C.M. Evidence from detrital zircons for the existence of continental crust and oceans on the Earth 4.4 Gyr ago. *Nature* **2001**, *409*, 175–178. [[CrossRef](#)] [[PubMed](#)]
4. Bowring, S.A.; Williams, I.S. Priscoan (4.00–4.03 Ga) orthogneisses from northwestern Canada. *Contrib. Mineral. Petrol.* **1999**, *134*, 3–16. [[CrossRef](#)]
5. Reimink, J.R.; Davies, J.H.F.L.; Chacko, T.; Stem, R.A.; Heaman, L.M.; Sarkar, C.; Schaltegger, U.; Creasser, R.A.; Pearson, D.G. No evidence for Hadean continental crust within Earth's oldest evolved rock unit. *Nat. Geosci.* **2016**, *9*, 777–780. [[CrossRef](#)]
6. Nutman, A.P.; Friend, C.R.L.; Bennett, V.C. Review of the oldest (4400–3600 Ma) geological and mineralogical record: Glimpses of the beginning. *Episodes* **2001**, *24*, 93–101. [[CrossRef](#)]
7. Cates, N.L.; Mojzsis, S.J. Pre-3750 Ma supracrustal rocks from the Nuvvuagittuq supracrustal belt, northern Quebec. *Earth Planet. Sci. Lett.* **2007**, *255*, 9–21. [[CrossRef](#)]
8. Liu, D.Y.; Nutman, A.P.; Compston, W.; Wu, J.S.; Shen, Q.H. Remnants of  $\geq 3800$  Ma crust in the Chinese part of the Sino-Korean craton. *Geology* **1992**, *20*, 339–342. [[CrossRef](#)]
9. Wan, Y.S.; Xie, H.Q.; Wang, H.C.; Liu, S.J.; Chu, H.; Xiao, Z.B.; Li, Y.; Hao, G.M.; Li, P.C.; Dong, C.Y.; et al. Discovery of early Eoarchean-Hadean zircons in eastern Hebei, North China Craton. *Acta Geol. Sin.* **2021**, *95*, 277–291.
10. Condie, K.C. *Developments in Precambrian Geology 3: Archean Greenstone Belts*; Elsevier: Amsterdam, The Netherlands, 1981.
11. Collins, W.J.; Van Kranendonk, M.J.; Teyssier, C. Partial convective overturn of Archean crust in the east Pilbara Craton, Western Australia: Driving mechanisms and tectonic implications. *J. Struct. Geol.* **1998**, *20*, 1405–1424. [[CrossRef](#)]
12. Lin, S.F.; Beakhouse, G.P. Synchronous vertical and horizontal tectonism at latest ages of Archean cratonization and genesis of Hemlo gold deposit, Superior craton, Ontario, Canada. *Geology* **2013**, *41*, 359–362. [[CrossRef](#)]
13. Wu, J.S.; Geng, Y.S.; Shen, Q.H.; Wan, Y.S.; Liu, D.Y.; Song, B. *Archean Geological Characteristics and Tectonic Evolution of the China-Korea Palecontinent*; Geological Publishing House: Beijing, China, 1998.
14. Geng, Y.S.; Liu, F.L.; Yang, C.H. Magmatic event at the end of the Archean in Eastern Hebei Province and its geological implication. *Acta Geol. Sin.* **2006**, *80*, 819–833.
15. Zhao, G.C.; Zhai, M.G. Lithotectonic elements of Precambrian basement in the North China Craton: Review and tectonic implications. *Gondwana Res.* **2013**, *23*, 1207–1240. [[CrossRef](#)]
16. Zhao, G.C. Metamorphic P-T paths of the eastern Hebei, western Shandong, Fuping, Wutai, and Hengshan domains, North China craton. In *Tectonothermal Evolution of the Basement Rocks of the North China Craton*; Lu, L.Z., Ed.; The college of Earth Sciences: Changchun, China, 1995; pp. 11–48. (In Chinese)
17. Wang, C.Q.; Cui, W.Y. Granulites from the Dengchang-Houshan area, northern Hebei Province: Geochemistry and metamorphism. In *Geological Evolution of the Granulite Terrain in the Northern part of the North China Craton*; Qian, X.L., Wang, R.M., Eds.; Seismological Press: Beijing, China, 1994; pp. 166–175. (In Chinese)
18. Chen, N.S.; Wang, R.J.; Shan, W.Y.; Zhong, Z.Q. Isobaric cooling P-T-t path of the western section of the Miyun Complex and its tectonic implications. *Sci. Geol. Sin.* **1994**, *29*, 354–364. (In Chinese)
19. Zhang, H.C.; Liu, J.H.; Chen, Y.C.; Zhang, Q.W.; Peng, T.; Li, Z.M.; Wu, C.M. Neoproterozoic metamorphic evolution and geochronology of the Miyun metamorphic complex, North China Craton. *Precambrian Res.* **2018**, *320*, 78–92. [[CrossRef](#)]
20. Liu, T.; Wei, C.J.; Johnson, T.; Sizova, E. Newly-discovered ultra-high temperature granulites from the East Hebei Terrane, North China Craton. *Sci. Bull.* **2022**, *67*, 670–673. [[CrossRef](#)]
21. Zhao, G.C.; Wilde, S.A.; Cawood, P.A.; Lu, L.Z. Thermal evolution of Archean basement rocks from the eastern part of the North China Craton and its bearing on tectonic setting. *Int. Geol. Rev.* **1998**, *40*, 706–721. [[CrossRef](#)]
22. Liu, T.; Wei, C.J.; Kröner, A.; Han, B.F.; Duan, Z.Z. Metamorphic P-T paths for the Archean Caozhuang supracrustal sequence, eastern Hebei Province, North China Craton: Implications for a sagduction regime. *Precambrian Res.* **2020**, *340*, 105346. [[CrossRef](#)]
23. Wan, Y.S.; Song, B.; Yang, C.; Liu, D.Y. Zircon SHRIMP UePb geochronology of Archean rocks from the FushuneQingyuan Area, Liaoning Province and its geological significance. *Acta Geol. Sin.* **2005**, *79*, 78–87. (In Chinese)
24. Wan, Y.S.; Song, B.; Yang, C.; Liu, D.Y. Geochemical Characteristics of Archean Basement in the FushuneQingyuan Area, Northern Liaoning Province and its geological significance. *Geol. Rev.* **2005**, *51*, 128–137. (In Chinese)
25. Peng, P.; Wang, C.; Wang, X.P.; Yang, S.Y. Qingyuan high-grade granite-greenstone terrain in the Eastern North China Craton: Root of a Neoproterozoic arc. *Tectonophysics* **2015**, *662*, 7–21. [[CrossRef](#)]
26. Wu, M.L.; Lin, S.F.; Wan, Y.S.; Gao, J.F. Crustal evolution of the Eastern Block in the North China Craton: Constraints from zircon U-Pb geochronology and Lu-Hf isotopes of the Northern Liaoning Complex. *Precambrian Res.* **2016**, *275*, 35–47. [[CrossRef](#)]

27. Li, Z.; Wei, C. Two types of Neoproterozoic basalts from Qingyuan greenstone belt, North China Craton: Petrogenesis and tectonic implications. *Precambrian Res.* **2017**, *292*, 175–193. [[CrossRef](#)]
28. Wu, D.; Wei, C.J. Metamorphic evolution of two types of garnet amphibolite from the Qingyuan terrane, North China Craton: Insights from phase equilibria modelling and zircon dating. *Precambrian Res.* **2021**, *355*, 106091. [[CrossRef](#)]
29. Li, Z.; Wei, C.; Chen, B.; Yang, F.; Zhang, X.; Cui, Y. Late Neoproterozoic high-grade regional metamorphism in the eastern North China Craton: New constraints from monazite dating in northern Liaoning. *Precambrian Res.* **2022**, *373*, 106625. [[CrossRef](#)]
30. Wu, K.K.; Zhao, G.C.; Sun, M.; Yin, C.Q.; He, Y.H.; Tam, P.Y. Metamorphism of the northern Liaoning Complex: Implications for the tectonic evolution of Neoproterozoic basement of the Eastern Block, North China Craton. *Geosci. Front.* **2013**, *4*, 305–320. [[CrossRef](#)]
31. Zhai, M.G.; Yang, R.Y.; Lu, W.J.; Zhou, J. Geochemistry and evolution of the Qingyuan Archaean granite–greenstone terrain, NE China. *Precambrian Res.* **1985**, *27*, 37–62. [[CrossRef](#)]
32. Zhao, G.C.; Sun, M.; Wilde, S.A.; Li, S.Z. Late Archaean to Paleoproterozoic evolution of the North China Craton: Key issues revisited. *Precambrian Res.* **2005**, *136*, 177–202. [[CrossRef](#)]
33. Tam, P.Y.; Zhao, G.C.; Sun, M.; Li, S.Z.; Wu, M.L.; Yin, C.Q. Petrology and metamorphic P-T path of high-pressure mafic granulites from the Jiaobei massif in the Jiao-Liao-Ji Belt, North China Craton. *Lithos* **2012**, *155*, 94–109. [[CrossRef](#)]
34. Qian, J.H.; Wei, C.J. P–T–t evolution of garnet amphibolites in the Wutai–Hengshan area, North China Craton: Insights from phase equilibria and geochronology. *J. Metamorph. Geol.* **2016**, *34*, 423–446. [[CrossRef](#)]
35. Wang, F.; Li, X.P.; Chu, H.; Zhao, G.C. Petrology and metamorphism of khondalites from Jining Complex in the North China Craton. *Int. Geol. Rev.* **2011**, *53*, 212–229. [[CrossRef](#)]
36. Wan, Y.S.; Xie, H.Q.; Wang, H.C.; Li, P.C.; Chu, H.; Xiao, Z.B.; Dong, C.Y.; Liu, S.J.; Li, Y.; Hao, G.M.; et al. Discovery of ~3.8 Ga TTG rocks in eastern Hebei, North China Craton. *Acta Geol. Sin.* **2021**, *95*, 1321–1333.
37. Zhao, G.C.; Cawood, P.A.; Li, S.Z.; Wilde, S.A.; Sun, M.; Zhang, J.; He, Y.H.; Yin, C.Q. Amalgamation of the North China Craton: Key issues and discussion. *Precambrian Res.* **2012**, *222*, 55–76. [[CrossRef](#)]
38. Shen, E.F.; Luo, H.; Han, G.G.; Dai, X.Y.; Jin, W.S.; Hu, X.D.; Li, S.B.; Bi, S.Y. *Archean Geology and Mineralization of Northern Liaoning and Southern Jilin Province*; Geological Publishing House: Beijing, China, 1994; pp. 1–255. (In Chinese)
39. Wang, K.; Liu, S.W.; Wang, M.J.; Yan, M. Geochemistry and zircon U–Pb–Hf isotopes of the late Neoproterozoic granodiorite–monzogranite–quartz syenite intrusions in the Northern Liaoning Block, North China Craton: Petrogenesis and implications for geodynamic processes. *Precambrian Res.* **2017**, *295*, 151–171. [[CrossRef](#)]
40. Duan, Z.Z.; Wei, C.J.; Li, Z. Metamorphic P–T paths and zircon U–Pb ages of Paleoproterozoic metabasic dykes in eastern Hebei and northern Liaoning: Implications for the tectonic evolution of the North China Craton. *Precambrian Res.* **2019**, *326*, 124–141. [[CrossRef](#)]
41. Pettijohn, F.J.; Chapter, S. *Chemical Composition of Sandstones Excluding Carbonate and Volcanic Sands*; US Government Printing Office: Washington, DC, USA, 1963; pp. S6–S7.
42. Mackie, W. Seventy chemical analyses of rocks. *Trans. Edinb. Geol. Soc.* **1899**, *8*, 33–60. [[CrossRef](#)]
43. Holland, T.J.B.; Powell, R. An improved and extended internally consistent thermodynamic dataset for phases of petrological interest, involving a new equation of state for solids. *J. Metamorph. Geol.* **2011**, *29*, 333–383. [[CrossRef](#)]
44. Duan, Z.Z.; Wei, C.J.; Rehman, H.U. Metamorphic evolution and zircon ages of pelitic granulites in eastern Hebei, North China Craton: Insights into the regional Archaean P–T–t history. *Precambrian Res.* **2017**, *292*, 240–257. [[CrossRef](#)]
45. White, R.W.; Powell, R.; Holland, T.J.B.; Johnson, T.E.; Green, E.C.R. New mineral activity–composition relations for thermodynamic calculations in metapelitic systems. *J. Metamorph. Geol.* **2014**, *32*, 261–286. [[CrossRef](#)]
46. Holland, T.J.B.; Powell, R. Activity–composition relations for phases in petrological calculations: An asymmetric multicomponent formulation. *Contrib. Mineral. Petrol.* **2003**, *145*, 492–501. [[CrossRef](#)]
47. White, R.W.; Powell, R.; Holland, T.J.B.; Worley, B.A. The effect of TiO<sub>2</sub> and Fe<sub>2</sub>O<sub>3</sub> on metapelitic assemblages at greenschist and amphibolite facies conditions: Mineral equilibria calculations in the system K<sub>2</sub>O–FeO–MgO–Al<sub>2</sub>O<sub>3</sub>–SiO<sub>2</sub>–H<sub>2</sub>O–TiO<sub>2</sub>–Fe<sub>2</sub>O<sub>3</sub>. *J. Metamorph. Geol.* **2000**, *18*, 497–511. [[CrossRef](#)]
48. Whitney, D.L.; Evans, B.W. Abbreviations for names of rock-forming minerals. *Am. Mineral.* **2010**, *95*, 185–187. [[CrossRef](#)]
49. Cherniak, D.J.; Zhang, X.Y.; Nakamura, M.; Watson, E.B. Oxygen diffusion in monazite. *Earth Planet. Sci. Lett.* **2004**, *226*, 161–174. [[CrossRef](#)]
50. Wu, Y.B.; Wang, H.; Gao, S.; Hu, Z.C.; Liu, X.C.; Gong, H.J. LA–ICP–MS monazite U–Pb age and trace element constraints on the granulite–facies metamorphism in the Tongbai orogen, central China. *J. Asian Earth Sci.* **2014**, *82*, 90–102. [[CrossRef](#)]
51. Rubatto, D.; Hermann, J.; Buick, I. Temperature and bulk composition control on the growth of monazite and zircon during low–pressure anatexis (Mount Stafford, central Australia). *J. Petrol.* **2006**, *47*, 1973–1996. [[CrossRef](#)]
52. Liu, Y.; Hu, Z.; Gao, S.; Günther, D.; Xu, J.; Gao, C.; Chen, H. In situ analysis of major and trace elements of anhydrous minerals by LA–ICP–MS without applying an internal standard. *Chem. Geol.* **2008**, *257*, 34–43. [[CrossRef](#)]
53. Liu, Y.S.; Hu, Z.C.; Zong, K.Q.; Gao, C.G.; Gao, S.; Xu, J.; Chen, H.H. Reappraisal and refinement of zircon U–Pb isotope and trace element analyses by LA–ICP–MS. *Chin. Sci. Bull.* **2010**, *55*, 1535–1546. [[CrossRef](#)]
54. Ludwig, K.P. *ISOPLOT: A Geochronological Toolkit for Microsoft Excel*; Geochronology Center Special Publication: Berkeley, CA, USA, 2003.

55. Sun, S.S.; McDonough, W.F. *Chemical and Isotopic Systematics of Oceanic Basalts: Implications for Mantle Composition and Processes*; Geological Society London Special Publications: Bath, UK, 1989; Volume 42, pp. 313–345.
56. Stevens, G.; Clemens, J.D.; Droop, G.T.R. Melt production during granulite facies anatexis: Experimental data from “primitive” metasedimentary protoliths. *Contrib. Mineral. Petrol.* **1997**, *128*, 352–370. [[CrossRef](#)]
57. Tajčmanová, L.; Connolly, J.A.D.; Cesare, B. A thermodynamic model for titanium and ferric iron solution in biotite. *J. Metamorph. Geol.* **2009**, *27*, 153–165. [[CrossRef](#)]
58. Hensen, B.J.; Osanai, Y. Experimental study of dehydration melting of F bearing biotite in model pelitic compositions. *Mineral. Mag. A* **1994**, *58*, 410–411. [[CrossRef](#)]
59. Petö, P. An experimental investigation of melting relations involving muscovite and paragonite in the silica-saturated portion of the system  $K_2O-Na_2O-Al_2O_3-SiO_2-H_2O$  to 15 kb total pressure. In *Progress in Experimental Petrology*; NERC: London, UK, 1976; pp. 41–45.
60. Holdaway, M.J. Application of new experimental and garnet Margules data to the garnet–biotite geothermometer. *Am. Mineral.* **2000**, *85*, 881–892. [[CrossRef](#)]
61. Wu, C.M.; Zhang, J.; Ren, L.D. Empirical garnet–biotite–plagioclase–quartz (GBPQ) geobarometry in medium- to high-grade metapelites. *Lithos* **2004**, *78*, 319–332. [[CrossRef](#)]
62. Wu, C.M.; Chen, H.X. Revised Ti-in-biotite geothermometer for ilmenite- or rutile-bearing crustal metapelites. *Sci. Bull.* **2015**, *60*, 116–121. [[CrossRef](#)]
63. Spear, F.S.; Florence, F.P. Thermobarometry in granulites: Pitfalls and new approaches. *Precambrian Res.* **1992**, *55*, 209–241. [[CrossRef](#)]
64. Kwan, L.C.J.; Zhao, G.C.; Yin, C.Q.; Geng, H.Y. Metamorphic P-T path of mafic granulites from Eastern Hebei: Implications for the Neoproterozoic tectonics of the Eastern Block, North China Craton. *Gondwana Res.* **2016**, *37*, 20–38. [[CrossRef](#)]
65. Liu, T.; Wei, C.J. Metamorphic evolution of Archean ultrahigh-temperature mafic granulites from the western margin of Qian’an gneiss dome, eastern Hebei Province, North China Craton: Insights into the Archean tectonic regime. *Precambrian Res.* **2018**, *318*, 170–187. [[CrossRef](#)]
66. Liu, T.; Wei, C.J. Metamorphic P-T paths and Zircon U–Pb ages of Archean ultra-high temperature paragneisses from the Qian’an gneiss dome, East Hebei terrane, North China Craton. *J. Metamorph. Geol.* **2020**, *38*, 329–356. [[CrossRef](#)]
67. Johannes, W.; Holtz, F. *Petrogenesis and Experimental Petrology of Granitic Rocks*; Springer: Berlin/Heidelberg, Germany, 1996; p. 335.
68. Robertson, J.K.; Wyllie, P.J. Experimental studies on rocks from the Deboullie Stock, Northern Maine, including melting relations in the water-deficient environment. *J. Geol.* **1971**, *79*, 549–571. [[CrossRef](#)]
69. Wei, C.J.; Guan, X.; Dong, J. HT-UHT metamorphism of metabasites and the petrogenesis of TTGs. *Acta Petrol. Sin.* **2017**, *33*, 1381–1404, (In Chinese with English Abstract).
70. Thompson, A.B.; England, P.C. Pressure temperature–time paths of regional metamorphism, II. Their influences and interpretation using mineral assemblages in metamorphic rocks. *J. Petrol.* **1984**, *25*, 929–955. [[CrossRef](#)]
71. Wells, P.R.A. Thermal models for magmatic accretion and subsequent metamorphism of continental crust. *Earth Planet. Sci. Lett.* **1980**, *46*, 253–265. [[CrossRef](#)]
72. Bohlen, S.R. On the formation of granulites. *J. Metamorph. Geol.* **1991**, *9*, 223–229. [[CrossRef](#)]
73. Zhao, G.C.; Wilde, S.A.; Cawood, P.A.; Lu, L.Z. Thermal evolution of two textural types of mafic granulites in the North China Craton: Evidence for both mantle plume and collisional tectonics. *Geol. Mag.* **1999**, *136*, 223–240. [[CrossRef](#)]
74. Sizova, E.; Gerya, T.; Stüwe, K.; Brown, M. Generation of felsic crust in the Archean: A geodynamic modeling perspective. *Precambrian Res.* **2015**, *271*, 198–224. [[CrossRef](#)]
75. Li, J.J.; Shen, B.F. Geochronology of Precambrian continental crust in Liaoning Province and Jilin Province. *Progress Precambrian Res.* **2000**, *23*, 249–255, (In Chinese with English Abstract).
76. Bai, X.; Liu, S.W.; Yan, M.; Zhang, L.F.; Wang, W.; Guo, R.R.; Guo, B.R. Geological event series of Early Precambrian metamorphic complex in South Fushun area, Liaoning Province. *Acta Petrol. Sin.* **2014**, *30*, 2905–2924, (In Chinese with English Abstract).
77. Wang, W.; Liu, S.W.; Cawood, P.A.; Bai, X.; Guo, R.R.; Guo, B.R.; Wang, K. Late Neoproterozoic subduction-related crustal growth in the Northern Liaoning region of the North China Craton: Evidence from ~2.55 to 2.50 Ga granitoid gneisses. *Precambrian Res.* **2016**, *281*, 200–223. [[CrossRef](#)]
78. Wang, M.J.; Liu, S.W.; Wang, W.; Wang, K.; Yan, M.; Guo, B.R.; Bai, X.; Guo, R.R. Petrogenesis and tectonic implications of the Neoproterozoic North Liaoning tonalitic-trondhjemitic gneisses of the North China Craton, North China. *J. Asian Earth Sci.* **2016**, *131*, 12–39. [[CrossRef](#)]
79. Wang, W.; Cawood, P.A.; Liu, S.W.; Guo, R.R.; Bai, X.; Wang, K. Cyclic formation and stabilization of Archean lithosphere by accretionary orogenesis: Constraints from TTG and potassic granitoids, North China Craton. *Tectonics* **2017**, *36*, 1724–1742. [[CrossRef](#)]
80. Wang, K.; Liu, S.W.; Wang, M.J.; Wang, W.; Yan, M. Formation ages, petrogenesis and geological implications of the Archean granitoid rocks in the Xinbin-Weiziyu Area, northern Liaoning Province. *Acta Sci. Nat. Univ. Pekin.* **2018**, *54*, 61–79, (In Chinese with English Abstract).

81. Peng, Z.D.; Wang, C.L.; Zhang, L.C.; Zhu, M.T.; Tong, X.X. Geochemistry of metamorphosed volcanic rocks in the Neoproterozoic Qingyuan greenstone belt, North China Craton: Implications for geodynamic evolution and VMS mineralization. *Precambrian Res.* **2019**, *365*, 196–211. [[CrossRef](#)]
82. Li, Z.; Wei, C.J.; Chen, B.; Zhang, W.; Yang, F. U–Pb–Hf–O–Nd isotopic and geochemical constraints on the origin of Archean TTG gneisses from North China Craton: Implications for crustal growth. *Precambrian Res.* **2021**, *354*, 106078. [[CrossRef](#)]